PCCP

Accepted Manuscript

ROYAL SOCIETY OF CHEMISTRY

www.rsc.org/pccp

Physical Chemistry Chemical Physics
CREATED USING THE RSC LaTeX PCCP ARTICLE TEMPLATE – SEE www.rsc.org/electronicfiles FOR DETAILS
ARTICLE TYPE www. rsc.org/xxxxxx | XXXXXXXX

In-situ oxidation study of Pd-Rh nanoparticles on $MgAl_2O_4(001)$

Patrick Müller,[a,c] Uta Hejral,[a,b,c] Uta Rütt,[a] and Andreas Stierle [*a,b,c]

Received Xth XXXXXXXXXX 20XX, Accepted Xth XXXXXXXXX 20XX
First published on the web Xth XXXXXXXXXX 200X
DOI: 10.1039/b000000x

Alloy nanoparticles on oxide supports are widely used as heterogeneous catalysts in reactions involving oxygen. Here we discuss the oxidation behavior of Pd-Rh alloy nanoparticles on $MgAl_2O_4(001)$ supports with a particle diameter from 6 - 11 nm. As an in-situ tool, we employed high energy grazing incidence x-ray diffraction at a photon energy of 85 keV. We find that physical vapor deposited Pd-Rh nanoparticles grow epitaxially on $MgAl_2O_4(001)$ with a truncated octahedral shape over the whole concentration range. During our systematic oxidation experiments performed at 670 K in the pressure range from 10^{-3} to 0.1 mbar, we observe for Rh containing nanoparticles the formation of two different Rh oxide phases, namely RhO_2 and a spinel-like Rh_3O_4 phase. PdO formation is only observed for pure Pd nanoparticles. This oxidation induced segregation behavior is also reflected in the oxidation induced enlargement of the average nanoparticle lattice parameter towards to value for pure Pd. Our results have ramifications for the phase separation behavior of alloy nanocatalysts under varying reducing and oxidizing environments.

1 Introduction

Alloy nanoparticles play an important role in heterogeneous catalysis because they may exhibit higher activity than catalysts composed of the individual materials, as reported recently for a number of systems[1,2]. For Pd-Rh nanoparticles it was shown that the turnover frequency for CO oxidation is highest at a composition of $Pd_{50}Rh_{50}$ and it was proposed that Pd-Rh interfaces play an important role in this enhanced activity[3,4]. Because of the complex heterogeneity of the involved materials at different length scales it is however unclear, what the microscopic origin of such enhanced activity may be: novel electronic states at alloy surfaces, particle size and shape dependent segregation behaviour or substrate induced segregation and strain effects. For alloys such as Pd-Rh and Pt-Rh bulk equilibrium phase diagrams predict phase separation below temperatures of about 1000-1200 K over a wide concentration range; experimentally this equilibrium is difficult to obtain and the formation of samples with mixed fcc structure is reported[5,6]. Catalyst nanoparticles are typically prepared and operated at temperatures significantly below the phase separation temperature, which makes it likely that phase separation occurs during their operation, transforming them from a mixed alloy into a bimetallic system with unknown spatial distribution of the elements. In technologically relevant processes like CO oxidation in car exhausts, Pd-Rh or Pt-Rh particles are exposed to alternating oxidative and reductive conditions. In this case preferential oxidation and surface segregation of the more reactive component may take place[7–9], triggering phase separation and the formation of Pd-Rh boundaries exposed to the surface with specific morphology.

To elucidate the concentration dependent oxidation behavior of Pd-Rh we grew epitaxial Pd-Rh nanoparticles on $MgAl_2O_4(001)$ with varying composition in a particle size range from 6 nm to 11 nm. The use of epitaxial nanoparticles on single crystal oxide supports as model systems has the advantage of a more uniform shape and size distribution and a well defined interface to the support, as compared to wet-chemically prepared powder catalysts[10]. Using grazing incidence x-ray diffraction as an in-situ tool allows us to obtain information on nanoparticle size, shape, lattice constants, as well as on the formed oxide phases under relevant near atmospheric oxygen pressures and elevated temperatures[11,12]. The use of photon energies in the 80 keV regime in combination with a large 2D detector gives in addition the opportunity of a distortion-free exploration of a large section of reciprocal space without sample or detector scanning[13,14]. Auxiliary scanning electron microscopy after the oxidation confirms the nanoparticle morphology of the sample and gives information upon the lateral particle size distribution and the average particle diameter.
As we will demonstrate, Pd-Rh nanoparticles on $MgAl_2O_4(001)$ grow predominantly with cube-on-cube epitaxy over the whole concentration range in the form of truncated octahedral nanoparticles. The oxidation process itself is governed by the formation of two different epitaxial

[a] *Deutsches Elektronen Synchrotron DESY, Notkestr. 85, 22607 Hamburg, Germany.*
[b] *Universität Hamburg Fachbereich Physik, Jungiusstr. 9, 20355 Hamburg, Germany.*
[c] *Universität Siegen Department Physik, Walter-Flex-Str. 3 , 57068 Siegen, Germany.*

Rh oxides for Rh containing particles, involving Rh surface segregation. Only for pure Pd nanoparticles the formation of PdO is observed. From the change of the average lattice parameter we deduced the oxidation induced change in Rh concentration in the metallic particle core. The paper is organized as follows: in the first section we will present the experimental details and the principles of our combinatorial high energy x-ray diffraction approach. Subsequently, the experimental data will be presented together with a quantitative analysis of the particle morphology and an assignment of the formed oxide phases. Moreover, our analysis of oxidation induced changes in concentration will be considered. The paper closes with the discussion and conclusion section.

2 Experimental Details

For the sample preparation we used $MgAl_2O_4$ (001) substrates with a size of 10 x 10 mm^2 and edges cut along $\langle 100 \rangle$ direction. The substrate had the normal spinel structure with a lattice constant of 8.086 Å[15]. The oxide support was treated in an ultrahigh vacuum (UHV) preparation chamber by repeated sputtering with 1 keV Ar ions and annealing at 1300 K under 1×10^{-7} mbar oxygen atmosphere in order to obtain a chemically clean and atomically smooth surface[16]. Rhodium and palladium were deposited simultaneously by electron beam evaporation under UHV conditions at a substrate temperature of 693 ± 5 K. The composition was varied by adjusting the individual material fluxes and it was cross-checked by x-ray reflectivity measurements as described below. Using a slit mask in front of the sample a combinatorial sample with well-defined stripes of different Rh-Pd composition and nanoparticle size was grown. The 1 mm wide stripes were separated by a distance of 1.5 mm. We deposited five stripes of epitaxial alloy nanoparticles running along the substrate $\langle 011 \rangle$ direction with varying compositions (Rh, $Rh_{0.6}Pd_{0.4}$, $Rh_{0.34}Pd_{0.66}$, $Rh_{0.15}Pd_{0.85}$ and Pd). The nanoparticle diameter D varied from 6 -11 nm for pure Rh and Pd, respectively. For the in situ oxidation experiment the sample was mounted inside a mobile high pressure compatible UHV x-ray diffraction chamber and cleaned by hydrogen treatment at 1×10^{-5} mbar H_2 and 570 K[17]. Post-oxidation experiments by scanning electron microscopy (SEM) were performed using a ZEISS MERLIN instrument at an electron energy of 2.5 keV combined with N_2 charge compensation.

The measurements were performed at the Deutsches Elektronen-Synchrotron (DESY, Hamburg), PETRA III, using a hard x-ray microbeam at the Physics hutch of the high energy materials science beamline P07 equipped with a diffractometer for grazing incidence diffraction[18]. A photon energy of 85 keV was employed and an energy resolution of $\frac{\Delta E}{E} = 2 \times 10^{-3}$ was obtained by a Si(111) double crystal monochromator in bent Laue geometry. The beam was focused by a set of 72 compound refractive lenses (CRL) which produced a vertical and horizontal beam size (FWHM) of $3\mu m \times 40\mu m$ at the sample position, limiting the footprint of the beam onto one individual stripe. A schematic drawing of the experimental setup is shown in Fig. 1. The sample was translated perpendicular to the beam to probe stripes of different concentration under identical temperature and pressure conditions.

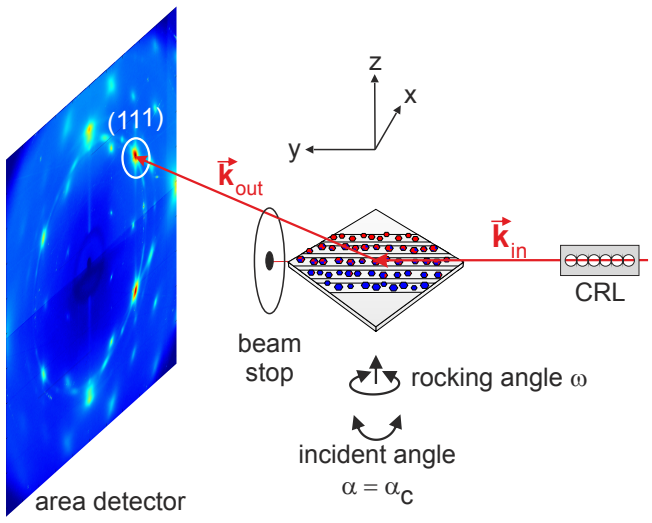

Fig. 1 Sketch of the experimental setup. To suppress the direct beam and powder rings from the beryllium window we used a beam stop and a circular mask directly behind the chamber. By moving the sample perpendicular to the beam (along x), different stripes with varying composition and particle size were probed.

We employed grazing incidence x-ray reciprocal space mapping using a two-dimensional (2D) Perkin-Elmer XRD 1621 detector. X-ray reflectivity data were recorded by a scintillation point detector equipped with a slit system and an automatic absorber system. The reflectivity data were deadtime, counting time and absorber corrected. For the reciprocal space mapping the incident angle was set to the critical angle for total external reflection of $MgAl_2O_4$ at 85 keV ($\alpha_c = 0.026°$), in order to reduce the signal from the substrate and to enhance the nanoparticle scattering signal. During the experiment the sample rocking angle ω was tuned to maximize the nanoparticle (111) Bragg signal, which is located in the reciprocal $(001)/(1\bar{1}0)$ plane.

Note that the nanoparticles exhibit an angular distribution $\Delta\omega$ around the surface normal of several degrees. This results in a scan in reciprocal space of considerable momentum transfer ΔQ because of the high photon energy employed[14]. As a consequence, for a sample with defined rotational disorder and finite crystalline domain size not only one spot in reciprocal space is probed, but a significant region around this spot. This implies for our sample that the crystal truncation rod signal from the particle facets or oxide phases with the

same azimuthal orientation but slightly different d-spacing can be probed simultaneously without rotating the sample around its surface normal. This diffraction scheme was recently successfully employed to determine single crystal surface structures during chemical reactions [14].

3 Experimental Results

3.1 Determination of the sample morphology

We performed x-ray reflectivity measurements to calibrate the surface coverage of the substrate. From the fit of the reflectivity data the electron density profile was determined. It contains as main information the averaged height of the particles and the average electron density of the nanoparticle containing layer, from which in turn the particle surface coverage and the amount of deposited material were determined [11]. Note that the integrated density profile representing the amount of deposited material is found to be independent from the details of the profile.

As an example, the x-ray reflectivity for the stripe with 34% Rh and 66% Pd is shown in Fig. 2a. The obtained electron density profile (inset Fig. 2a) is composed of two layers, representing well the true density profile given by the nanoparticle shape and their height distribution. By integration of the profile we yield a coverage of 36%.

Post experimental scanning electron microscopy experiments (as an example for nanoparticles with $Rh_{0.15}Pd_{0.85}$ composition, see Fig. 2b) evidence the presence of nanoparticles on the surface with an average lateral size of 11 nm and a large size distribution of 70%, which may be to some extent the result of the oxidation process (see below). Table 1 summarizes the results from the reflectivity measurements. The total coverage of the probed Pd-Rh compositions ranges from 33-40 %, and appears to be neither correlated with the alloy concentration nor the particle height.

Table 1 Summary of the fit results for the reflectivity measurements recorded at 670 K after hydrogen treatment and annealing under UHV conditions at a temperature of 870 K. As average particle height the sum of the thicknesses of layer 1 and 2 is given. Overall error bars are about 10% for both, composition and coverage.

nanoparticles	height (nm)	coverage (%)
Rh	3.1	39.5
$Rh_{0.60}Pd_{0.40}$	5.6	33.0
$Rh_{0.34}Pd_{0.66}$	5.8	36.3
$Rh_{0.15}Pd_{0.85}$	6.3	33.5
Pd	8.5	34.8

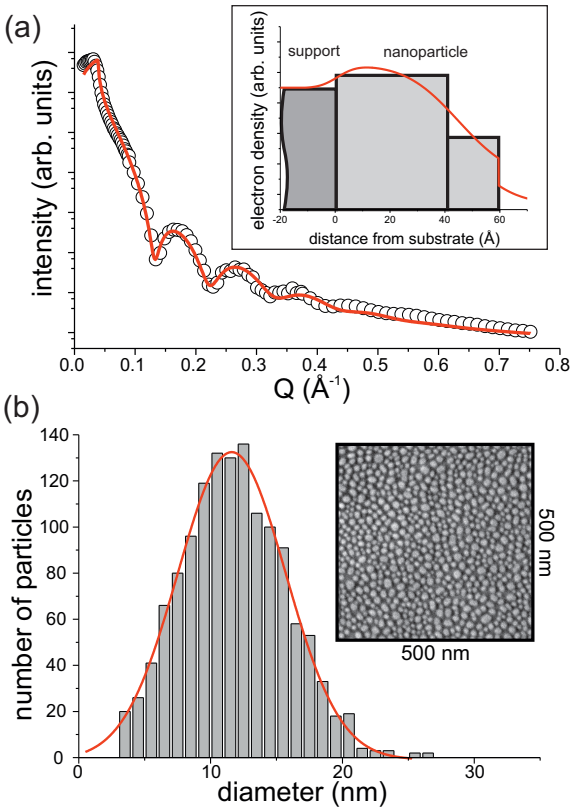

Fig. 2 (a) X-ray reflectivity from $Rh_{0.34}Pd_{0.66}$ nanoparticles at T = 670 K after hydrogen treatment and annealing under UHV conditions to 870 K (dots: experimental data, solid line: fit). Electron density profile with two layer box model (inset). (b) Size distribution determined from SEM image (inset) for $Rh_{0.15}Pd_{0.85}$ nanoparticles after oxidation in the mbar regime.

3.2 Nanoparticle epitaxy

During the experiment high energy reciprocal space maps were recorded with the sample rotation ω adjusted to the nanoparticle (111) Bragg reflection in the (001) / (110) reciprocal lattice plane of Rh, see Fig. 3 (a) and (b). Fig. 3 (c) gives an overview of the different reflections observed after annealing the sample at 870 K. The map in Fig. 3 (c) is dominated by the (111) reflections of (001) oriented nanoparticles in cube-on-cube epitaxy on the $MgAl_2O_4$ (001) surface for the whole concentration range under investigation. In addition, rod like diffraction streaks are detected in line with the truncated octahedral shape of this type of particles [13]. The faintness of signals from (111) and (110)-oriented particles and the absence of Debye Scherrer rings from randomly oriented particles further confirm the well-defined particle epitaxy. Moreover, diffraction signals from internal twinning of the (001) as well as (111) oriented particles along {111} type of planes are detected [13]. The observation of (111) and (110) oriented

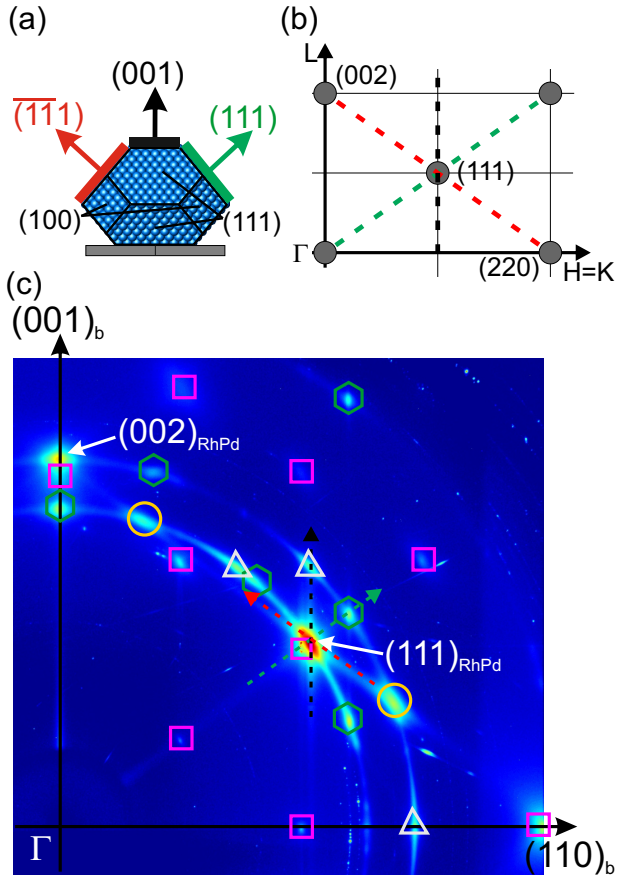

Fig. 3 (a) Schematic view of a $Rh_{0.60}Pd_{0.40}$ particle, the CTR signal of the different facets is indicated by arrows. (b) Reciprocal lattice of truncated octahedral nanoparticles in the (110)/(001) plane; the dashed lines indicate truncation rods from the {111} and {001} type nanoparticle facets. (c) High energy reciprocal space map for pure Pd nanoparticles recorded at T = 670 K. In addition to the (111) reflection from the particles also the (002) reflection is observed because of the wide orientation distribution of the particles. The additional reflections belong to $MgAl_2O_4$ (squares), (111)-oriented particles (hexagons), (110)-oriented particles (triangles) and internal twinning of (001) and (111) oriented particles (circles).

particles can be explained by a particle size dependent stabilization of different epitaxial relationships and growth directions [19]. The well defined epitaxy and predominant (001) particle orientation is maintained over the whole concentration range up to pure Rh, as recognized from inspection of Fig. 4, first line. The only apparent difference is the gradual disappearance of the signal from (111) oriented particles; from the present data it can, however, not be concluded if this behavior is due to the concentration variation or differences in the average particle size.

The average nanoparticle diameters D and heights H were determined by fitting of the linescans through the (111) Bragg reflections along the ⟨111⟩ and ⟨001⟩ directions; the results are summarized in Fig. 5. The full width at half maximum ΔQ (in $Å^{-1}$) of the line scans is connected by $B = \frac{2\pi}{\Delta Q}$ to the corresponding real space dimension B. The particles exhibit after annealing to 870 K heights and diameters between 6 nm and 11 nm, according to the varying amount of material deposited. The ratio H/D decreases systematically with increasing Pd concentration from 0.84 (pure Rh) to 0.74 for $Rh_{0.15}Pd_{0.85}$, but then it jumps back to 0.82 for pure Pd. This observation may be taken as an indication for Pd surface segregation in alloy particles under UHV annealing conditions. For Pd the difference between (100) and (111) surface energies is smaller, as compared to Rh, explaining a flatter particle shape. In the case of pure Pd, an increase in the interfacial energy can be held responsible for the change towards a more three-dimensional shape.

Furthermore, from the H/D ratio an upper limit of the adhesion energy E_{ad} for Pd and Rh on $MgAl_2O_4(001)$ can be estimated. The adhesion energy is related to the height $H_{T,B}$ of the top and bottom part of the particle via $E_{ad}=\gamma_{100}\cdot\frac{H_T-H_B}{H_T}$, where γ_{100} denotes the surface energy of the (100) surface [12,20]. For octahedral particles, the maximum ratio H_T/D is $1/\sqrt{2}$, resulting in an upper limit for E_{ad} for Rh of 125 meV/$Å^2$ and for Pd of 82 meV/$Å^2$, both in good agreement with adhesion energy values reported for Rh and Pd on MgO(001) [12,21].

3.3 Oxidation induced shape changes and bulk oxide formation

During the subsequent oxidation diffraction patterns were recorded for different oxygen pressures at a constant temperature of 670 K (see Fig. 4). The evolution of the average particle size, shape and lattice parameter was obtained from the fitting of linescans as described above. At 10^{-3} mbar and 670 K first changes were observed in the diffraction patterns: for the pure Pd particles a reduction in the {111} and {001} type facet truncation rod signal is observed, which is in line with a previously reported rounding of the particles and the formation of {112} type facets [21]. For the $Rh_{0.15}Pd_{0.85}$ particles only slight changes are visible. For higher Rh concentrations novel diffraction peaks can be observed in line with the formation of thicker bulk oxide layers or oxide nanoparticles. This observation is in agreement with a lowering of kinetic barriers for bulk oxide formation for Rh rich particles. It can, however, not be excluded that this more pronounced oxidation is partially related to the reduction in average particle size.

Only at a higher oxygen pressure of 10^{-1} mbar bulk oxide formation sets in also for pure Pd and $Rh_{0.15}Pd_{0.85}$ particles. In the case of pure Pd the particle reflections were detected at different positions as compared to Pd_xRh_{1-x} and pure Rh particles. For Rh containing particles the intensity of the reflections observed at lower pressures increased but no additional

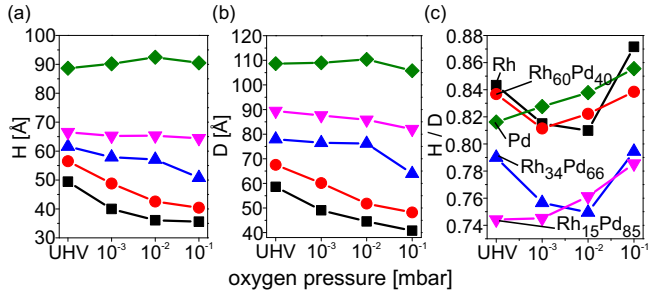

Fig. 5 Average nanoparticle height H (a) and diameter D (b) and ration H/D in (c) determined from reciprocal space maps as a function of oxygen pressure at 670 K. Data symbols correspond to: pure Rh (squares), $Rh_{0.60}Pd_{0.40}$ (circles), $Rh_{0.34}Pd_{0.66}$ (upward triangles), $Rh_{0.15}Pd_{0.85}$ (downward triangles), pure Pd (diamonds).

reflections were observed indicating that no additional oxide phase or orientation was formed. Since the oxide reflections are at identical positions for pure Rh and Pd_xRh_{1-x} particles, we argue that Rh oxide formation is the dominating process by oxygen induced outward segregation of Rh atoms. This assumption is moreover underlined by the fact that the oxide reflections are progressivley stronger for particles with increasing Rh concentration. Surprisingly, pronounced Debye-Scherrer rings from powderlike oxide with random orientation are absent for all compositions and oxygen pressures, indicating that oxide domains form either in epitaxy with the nanoparticle facets or with the spinel substrate.

The evolution of the nanoparticle average diameter and height during oxidation and the height to diameter ratio are presented in Fig. 5. For pure Pd particles they stays almost constant, while as a general trend it is observed that the oxidation induced relative decrease in particle size is enhanced for higher Rh concentrations and oxygen pressures, in line with the increase of the oxide signal discussed above. For the pure Rh as well as 60% and 34 % Rh rich nanoparticles the H/D ratio first decreases, as expected for an increase of the top (001) facet area. This observation can be explained by the energetically more favorable nucleation of surface oxide on Rh(100) as compared to Rh(111)[12,20].

For the highest oxygen pressure of 10^{-1} mbar this effect is reversed presumably due to higher oxidation rate of the (111) facets or anisotropic Rh segregation behavior. For the 15% Rh containing particles the relative decrease in H and D is much smaller and the ratio H/D is increasing as a function of oxygen pressure. Pure Pd shows a partially different behavior: initially a slight increase in the absolute values of H and D is observed (accompanied by a small decrease of the maximum Bragg peak intensity), which is in agreement with the preferential oxidation of smaller particles, shifting the average particle size to larger values[13]. For pure Pd the increase in H/D with increasing oxygen pressure is in agreement with the oxygen induced formation of {112} type facets as mentioned above, giving rise to a rounder particle shape[21].

Table 2 Experimental d-spacings and the d-spacings of the different rhodium oxides. Labels according to Fig. 6

Label in Figure	d_{exp} (Å)	Rh_3O_4	RhO_2	Rh_2O_3
1	3.012	(0 0 6)		
2	3.011			
3	2.558			(1 0 $\bar{1}$ 4)
4	2.554			
5	2.546	(1 0 2)	(1 0 1)	(1 1 $\bar{2}$ 0)
6	2.540			
7	2.365			(0 0 0 6)
8	2.286	(1 0 4)	(0 0 2)	(1 1 $\bar{2}$ 3)
9	2.284		(1 1 0)	
10	2.243			(2 0 $\bar{2}$ 2)
11	1.731			
12	1.730	(1 0 8)		(1 1 $\bar{2}$ 6)
13	1.544		(1 1 2)	
14	1.522	(0 0 12)	(2 0 0)	(0 1 $\bar{1}$ 8)
15	1.454	(1 0 10)		(3 0 $\bar{3}$ 0)

3.4 Identification of bulk oxide phases

As a next step, possible candidates for the bulk oxide phases compatible with the diffraction patterns observed for Rh containing and pure Pd particles are identified. As mentioned above, the diffraction patterns differ significantly for these two cases. We first discuss the diffraction pattern for $Rh_{0.6}Pd_{0.4}$ particles after oxidation at 670 K and 0.1 mbar O_2 pressure, which is representative for Rh containing particles (see Fig. 6a). The majority of the oxidation induced, additional reflections (compare to the UHV situation in Fig. 3) can be explained by the formation of a specific Rh oxide phase growing perpendicular to the low index (100) and (111) type facets in identical orientation, respectively, as pictured schematically in Fig. 6b.

From previous experiments on the near atmospheric pressure oxidation of Rh(100) surfaces, we know that at intermediate pressures and temperatures a transient epitaxial Rh oxide phase forms, which is neither compatible with rutile RhO_2 (a=3.09 Å and c = 4.49 Å) nor corundum Rh_2O_3 (a=5.13 Å, c=13.85 Å, from ref.[22]). Instead, it can be described by a hexagonal unit cell with $a = b = 6.16$ Å, $c = 17.7$ Å, $\alpha = \beta = 90°$ and $\gamma = 120°$[23]. Table 2 summarizes the d spacings of the reflections labeled in Fig. 6a and those of known Rh bulk oxide phases. The diffraction pattern is in line with an "ABC" stacking of the hexagonal closed-packed oxygen and partially occupied metal ion layers inside the unit cell, similar to a spinel structure in (111) orientation with $a = b = 6.15$ Å, $c = 18.07$ Å, close to the values observed for the Rh(100) sur-

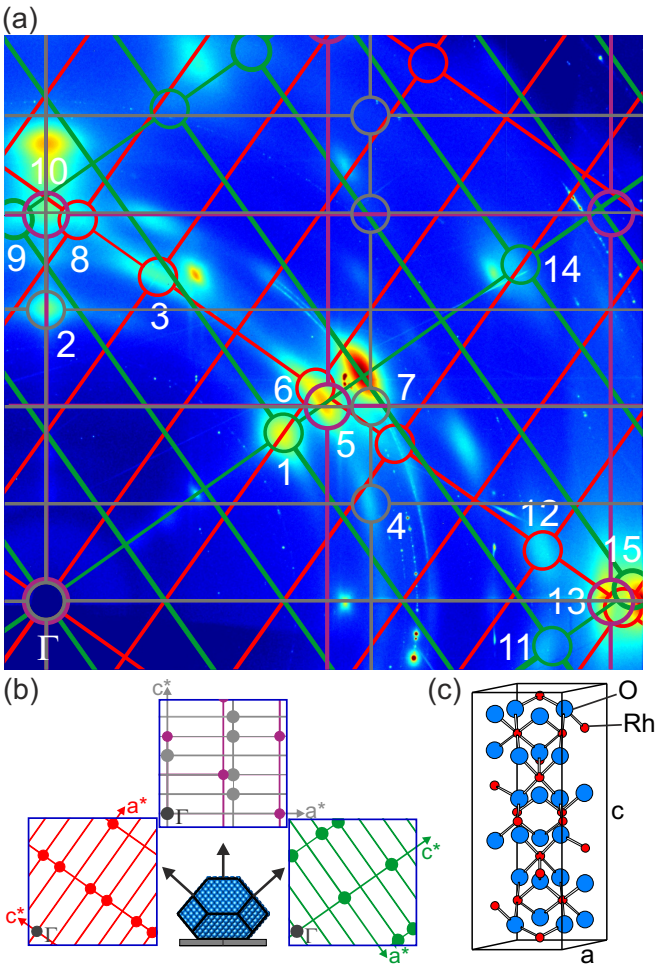

Fig. 6 (a) 2D diffraction pattern of $Rh_{0.6}Pd_{0.4}$ nanoparticles at 0.1 mbar of oxygen and a temperature of 670 K with reciprocal lattices and reflections for Rh_3O_4 and RhO_2. Strong reflections according to the bulk structure factors are indicated by larger circles. (b) sketch of a (001)-oriented particle showing the orientation of the Rh oxide reciprocal lattice with respect to the corresponding facets. Small circles indicate reflections from RhO_2. (c) hexagonal unit cell of a spinel like Rh oxide with lattice parameters a = 6.15 Åand c = 18.07 Å.

face. The found unit cell parameters match with an in-plane spinel structure with typical cubic lattice constants between $7.7 - 9\text{Å}$[24]. In out-of- plane direction the lattice is, however, expanded by 10 % as compared to the (cubic) spinel lattice constant that is derived from the in-plane lattice constants. Apparently, reflections 10 and 13, corresponding to d=2.24 Å and d=1.54 Å cannot be explained within this scheme. Comparing with d-spacings of reported bulk Rh oxide structures (see Table 2), it becomes evident, that the reflection labeled with 5 agrees well with the $(11\bar{2}0)$ d-spacing of α-Rh_2O_3 with corundum structure, or with the (101) reflection of RhO_2 with rutile structure. We argue that the formation of Rh_2O_3 can be ruled out because in this case additional reflections from a high symmetry reciprocal space plane containing the $(11\bar{2}0)$ reflection would be expected, which are absent. On the other hand, formation of RhO_2 with (001) direction perpendicular to the spinel substrate surface is compatible with the extra diffraction spots, as visualized by the RhO_2 reciprocal lattice (101) plane drawn in magenta in Fig. 6b.

For pure palladium nanoparticles the diffraction pattern looks distinctly different, as discussed above. The diffraction pattern presented in Fig. 7 obtained after oxidation at 670 K and 0.1 mbar O_2 pressure can be explained on the basis of tetragonal PdO with the lattice constants a = 3.03 Å and c = 5.33 Å[25]. In this structure Pd atoms sit on positions of a body centred tetragonal (bct) lattice and oxygen atoms occupy tetrahedral sites, resulting in a fourfold coordination of oxygen as well as Pd (see Fig. 7d). The reciprocal lattice of PdO is characterized by strong reflections dominated by the Pd bct sublattice, for which h+k+l (sum of PdO reciprocal lattice indices) yields an even number. In addition, weak reflections from the oxygen sublattice exist, for which h+k+l results in an odd number, while l is even[25].

Because for PdO the ratio c/a is very close to $\sqrt{3}$, the momentum transfer for certain reflections from the Pd sublattice is very close to each other (such as (002) and (101)). The orientation of the PdO lattice can therefore only be unambiguously deduced from the observation (or missing) of weaker (100) type reflections of the oxygen sublattice. Inspection of the diffraction pattern in Fig. 7 yields (100) reflections in pure in-plane and out-of-plane directions, which is compatible with (100) oriented PdO domains, either with in-plane (010) or (001) orientation, as pictured in Fig. 7b for reciprocal space and in Fig. 7d for real space. Most of the other PdO reflections can be explained by (100) oriented domains, which for this case turns out to be the predominant orientation. In addition, in the out-of-plane direction a weaker reflection is observed, which can be indexed as (002) or (101), corresponding to either (001) or (101) oriented domains. The (101) labeled reflection fits also to this orientation. Since we do not observe the corresponding (100) signal, which would be expected for (101) oriented domains (for comparison see Fig. 7c) we con-

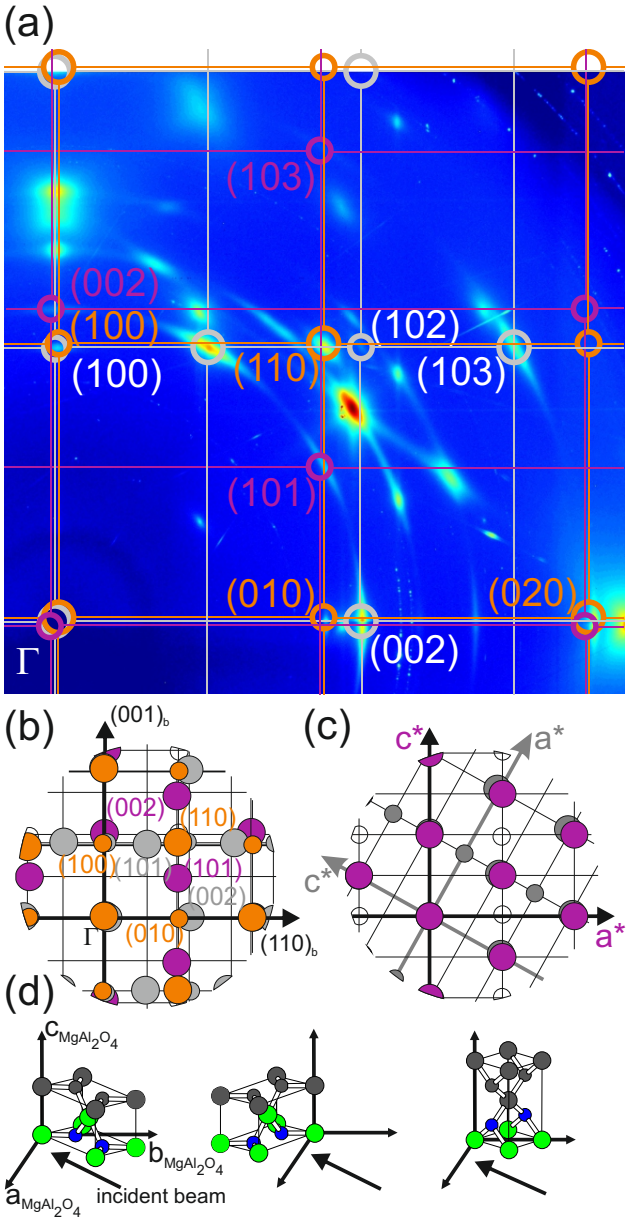

Fig. 7 (a) Experimental diffraction map for pure Pd nanoparticles at 670 K and 0.1 mbar oxygen pressure. Superimposed are reciprocal lattices from 2 inplane rotated (100) domains (orange and gray) and a (001) domain (magenta). (b) schematic representation of the reflections expected for (100) and (001) oriented domains, as shown in real space in (d). (c) superposition of reciprocal lattices of (001) and (101) oriented domains.

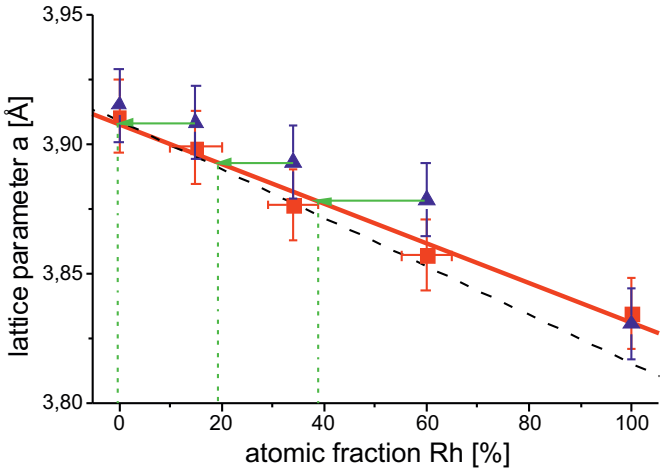

Fig. 8 Average lattice parameter as a function of the nominal composition. Squares: before oxidation, triangles: after oxidation. The solid line is a linear fit to the data before oxidation, the dashed line corresponds to Vegard's law for bulk Pd-Rh at 670 K. The bulk lattice constants of Pd and Rh at 670 K are 3.909 Åand 3.816 Å, respectively. The arrows indicate the nanoparticle metallic core composition after oxidation.

clude, that as second but minor orientation PdO (001) domains are present.

The observation of predominantly (100) orientated domains differs from our previous results on the oxidation of Pd nanoparticles of similar size on MgO(100), during which we observed (001) oriented domains only [11,13]. This supports our previous hypothesis, that PdO growth mainly takes place in contact with the substrate and not on the facets of the particles, mediated by an oxygen induced Pd diffusion process and / or complete oxidation of smaller particles. Accordingly, we did not observe oxide reflections corresponding to epitaxial oxide formed on top of the low index {111} facets of the Pd nanoparticles, at variance to the Rh containing particles.

3.5 Evolution of the particle composition during oxidation

Vegard's law describes the dependence of the lattice parameter on the alloy composition as a linear relationship, which is fulfilled in very good approximation for the system Pd-Rh [26]. The nominal composition of our samples was cross-checked by x-ray reflectivity measurements, yielding the total amount of material deposited for each stripe, as described in section 3.1. The deposition rate for the individual components was determined from the pure Rh and Pd stripes, respectively. The lattice parameter was deduced from the peak maximum of the radial scans through the (111) reflection using Bragg's law. In Fig. 8 the lattice parameter is plotted as a function of the initial composition before oxidation (filled squares) along with

a least mean square fit to the data, in good agreement with a linear relationship (solid line). This linear relationship does not exactly follow Vegard's law for bulk PdRh (dashed line in Fig. 8, including thermal expansion[27,28], *), which might be related to residual epitaxial strain more pronounced for the smaller Rh nanoparticles.

After oxidation at 0.1 mbar and 670 K, an intriguing evolution of the nanoparticle lattice parameter is observed for the alloy nanoparticles (see Fig. 8). Taking into account the linear relationship between the particle composition and the lattice parameter, the increase of the average lattice parameter upon oxidation can be interpreted in terms of a depletion in Rh, which is in line with the observed predominant formation of Rh oxide for all alloy nanoparticles. Notably, the $Rh_{0.15}Pd_{0.85}$ particles adopt after oxidation the Pd lattice parameter, within the error bars of our experiment. This implies that after oxidation their pure Pd core is surrounded by a Rh oxide shell, preventing further oxidation. For pure Pd and Rh, no oxidation induced change of the lattice parameter is observed.

4 Discussion and Conclusions

We have demonstrated that truncated octahedral, (001) oriented Pd-Rh nanoparticles can be grown over the full concentration range on $MgAl_2O_4(001)$ at 670 K by physical vapor deposition. In the bulk the system Pd-Rh is predicted to exhibit a miscibility gap below 1200 K over the whole concentration range[29] which is supported to some extent by experimental results[5]. On the other hand, the concentration dependence of the bulk lattice parameter was determined from samples prepared at $\sim$ 1600 K in the solid solution phase after quenching them to room temperature in order to maintain the state[26], which is only possible when the driving force for phase separation is low. At the surface of Pd rich alloy single crystals the segregation of Pd was reported after annealing under UHV conditions[30] in line with the lower surface energies of Pd as compared to Rh[20]. Thus, our PdRh alloy nanoparticles likely exhibit Pd surface segregation after annealing at 870 K prior to oxidation.

The tendency for phase separation in this system facilitates the observed oxygen induced Rh surface segregation and the formation of Rh bulk oxide, despite of the presumably initial Pd segregation. Likewise, Rh surface segregation is observed for Pd-Rh nanoparticles under CO oxidation conditions[3,8]. After oxidation of $Rh_{0.5}Pd_{0.5}$ nanoparticles with a diameter of 15 nm at 133 mbar and 493 K, x-ray photoemission gave evidence for the dominant formation of Rh oxide and some Pd oxide[3], which we did not observe in our study for Rh containing particles. This may be related to the lower oxygen pressures and / or to the smaller particle sizes employed in our study.

In a recent atom probe tomography study a PdRh alloy tip (6.4 at. % Rh) with $\sim$50 nm diameter was investigated after oxidation at 873 K and 1 bar oxygen pressure[31]. Mainly the formation of PdO and some mixed Pd-Rh oxides was observed, at variance to our observations. We may conlude again that the difference in oxidation conditions plays an important role, but also the difference in size and geometry between the 50 nm atom probe tip and our 10 nm particles allowing much easier exchange processes of atoms in the near surface region.

Finally we address the thermodynamics of the observed bulk oxide phases. The heat of formation of PdO, Rh_2O_3 and RhO_2 are 1.22 eV, 1.23 eV and 1.24 eV / oxygen atom, respectively, corresponding to oxygen pressures in the 10^{-5} mbar regime at 670 K[32–34]. This implies that Rh_2O_3, RhO_2 and PdO are expected to form in equilibrium under very similar conditions. Experimentally we find that the formation of a Rh_3O_4 spinel like phase and RhO_2 sets in at $\sim 10^{-3}$ mbar, whereas the formation of PdO for the pure Pd nanoparticles starts only at 0.1 mbar oxygen pressure, as also previously observed for different Pd single surfaces and Pd nanoparticles[11,32,35–37]. This points to an enhanced kinetic barrier for the formation of PdO as compared to the Rh oxides, which we argue is the reason for the selective oxidation observed for Pd-Rh alloy nanoparticles. We may speculate that these different kinetic barriers prevent Pd from oxidation during catalytic oxidation / reduction cycles. The observed spinel like Rh_3O_4 phase as well as RhO_2 may play an important role as active, oxygen supplying phase under reaction conditions, whereas Rh_2O_3 is not present under the conditions applied in this study.

Acknowledgments: We thank Olof Gutowski for his technical support during our beamtime at P07 (PETRA III). The ZEISS application laboratory is acknowledged for the conduction of the SEM experiments. Financial support by the Bundesministerium für Bildung und Forschung (BMBF), Project No. 05K10PS1 (NanoXcat) is gratefully acknowledged. The Max Planck Society (MPG) is acknowledged for technical support.

References

1 J. Y. Park, Y. Zhang, M. Grass, T. Zhang and G. A. Somorjai, *Nano Letters*, 2008, **8**, 673–677.
2 W. Chen and S. Chen, *Journal of Materials Chemistry*, 2011, **21**, 9169–9178.
3 J. R. Renzas, W. Huang, Y. Zhang, M. E. Grass, D. T. Hoang, S. Alayoglu, D. R. Butcher, F. F. Tao, Z. Liu and G. A. Somorjai, *Physical Chemistry Chemical Physics*, 2011, **13**, 2556–2562.
4 W. G. Menezes, B. Neumann, V. Zielasek, K. Thiel and M. Bumer, *ChemPhysChem*, 2013, **14**, 1577–1581.

* The alloy thermal expansion was calculated as a concentration dependent linear superposition of the thermal expansion coefficients of the individual constituents.

5 S. Tripathi and S. Bharadwqj, *Journal of Phase Equilibria*, 1994, **15**, 208–212.

6 H. Okamoto, *Journal of Phase Equilibria*, 1994, **15**, 369–369.

7 M. Grass, Y. Zhang, D. Butcher, J. Park, Y. Li, H. Bluhm, K. Bratlie, T. Zhang and G. Somorjai, *Angewandte Chemie International Edition*, 2008, **47**, 8893–8896.

8 F. Tao, M. E. Grass, Y. Zhang, D. R. Butcher, F. Aksoy, S. Aloni, V. Altoe, S. Alayoglu, J. R. Renzas, C.-K. Tsung, Z. Zhu, Z. Liu, M. Salmeron and G. A. Somorjai, *Journal of the American Chemical Society*, 2010, **132**, 8697–8703.

9 R. Westerström, J. G. Wang, M. D. Ackermann, J. Gustafson, A. Resta, A. Mikkelsen, J. N. Andersen, E. Lundgren, O. Balmes, X. Torrelles, J. W. M. Frenken and B. Hammer, *Journal of Physics: Condensed Matter*, 2008, **20**, 184018–184023.

10 C. R. Henry, *Surface Science Reports*, 1998, **31**, 231–325.

11 N. Kasper, A. Stierle, P. Nolte, Y. Jin-Phillipp, T. Wagner, D. de Oteyza and H. Dosch, *Surface Science*, 2006, **600**, 2860–2867.

12 P. Nolte, A. Stierle, N. Y. Jin-Phillipp, N. Kasper, T. U. Schulli and H. Dosch, *Science*, 2008, **321**, 1654–1658.

13 P. Nolte, A. Stierle, N. Kasper, N. Y. Jin-Phillipp, H. Reichert, A. Rühm, J. Okasinski, H. Dosch and S. Schöder, *Physical Review B*, 2008, **77**, 115444–1–115444–6.

14 J. Gustafson, M. Shipilin, C. Zhang, A. Stierle, U. Hejral, U. Ruett, O. Gutowski, P.-A. Carlsson, M. Skoglundh and E. Lundgren, *Science*, 2014, **343**, 758–761.

15 G. B. Andreozzi, F. Princivalle, H. Skogby and A. D. Giusta, *American Mineralogist*, 2000, **85**, 1164 – 1171.

16 M. K. Rasmussen, A. S. Foster, B. Hinnemann, F. F. Canova, S. Helveg, K. Meinander, N. M. Martin, J. Knudsen, A. Vlad, E. Lundgren, A. Stierle, F. Besenbacher and J. V. Lauritsen, *Physical Review Letters*, 2011, **107**, 036102–1–036102–4.

17 A. Kalinkin, A. Pashis and V. Bukhtiyarov, *Reaction Kinetics and Catalysis Letters*, 2003, **78**, 121–127.

18 H. Reichert, V. Honkimäki, A. Snigirev, S. Engemann and H. Dosch, *Physica B: Condensed Matter*, 2003, **336**, 46 – 55.

19 J. Goniakowski, A. Jelea, C. Mottet, G. Barcaro, A. Fortunelli, Z. Kuntov, F. Nita, A. C. Levi, G. Rossi and R. Ferrando, *The Journal of Chemical Physics*, 2009, **130**, 174703–1–174703–9.

20 F. Mittendorfer, N. Seriani, O. Dubay and G. Kresse, *Physical Review B*, 2007, **76**, 233413–1–233413–4.

21 P. Nolte, A. Stierle, N. Kasper, N. Y. Jin-Phillipp, N. Jeutter and H. Dosch, *Nano Letters*, 2011, **11**, 4697–4700.

22 J. M. D. Coey, *Acta Crystallographica Section B*, 1970, **26**, 1876–1877.

23 J. Gustafson, E. Lundgren and A. Stierle, *unpublished*.

24 K. E. Sickafus and J. M. Wills, *Journal of the American Ceramic Society*, 1999, **82**, 3279–3292.

25 J. Waser, H. A. Levy and S. W. Peterson, *Acta Crystallographica*, 1953, **6**, 661–663.

26 P. Franke and D. Neuschtz, in *Landolt-Börnstein - Group IV Physical Chemistry*, vol. 19B5.

27 H. P. Singh, *Acta Crystallographica Section A*, 1968, **24**, 469–471.

28 B. N. Dutta and B. Dayal, *Physica Status Solidi (b)*, 1963, **3**, 2253–2259.

29 K. Jacob, S. Priya and Y. Waseda, *Journal of Phase Equilibria*, 1998, **19**, 340–350.

30 J. Leiro, M. Heinonen and I. Batirev, *Applied Surface Science*, 1995, **90**, 515 – 521.

31 T. Li, P. A. J. Bagot, E. A. Marquis, S. C. E. Tsang and G. D. W. Smith, *The Journal of Physical Chemistry C*, 2012, **116**, 4760–4766.

32 N. Kasper, P. Nolte and A. Stierle, *The Journal of Physical Chemistry C*, 2012, **116**, 21459–21464.

33 T. H. Jacob, T. Uda, T. H. Okabe and Y. Waseda, *High Temperature Materials and Processes*, 2000, **19**, 11–16.

34 K. Jacob and D. Prusty, *Journal of Alloys and Compounds*, 2010, **507**, L17 – L20.

35 E. Lundgren, J. Gustafson, A. Mikkelsen, J. N. Andersen, A. Stierle, H. Dosch, M. Todorova, J. Rogal, K. Reuter and M. Scheffler, *Physical Review Letters*, 2004, **92**, 046101–1–046101–4.

36 R. Westerström, C. J. Weststrate, J. Gustafson, A. Mikkelsen, J. Schnadt, J. N. Andersen, E. Lundgren, N. Seriani, F. Mittendorfer, G. Kresse and A. Stierle, *Physical Review B*, 2009, **80**, 125431–1–125431–11.

37 R. Westerström, M. E. Messing, S. Blomberg, A. Hellman, H. Grönbeck, J. Gustafson, N. M. Martin, O. Balmes, R. van Rijn, J. N. Andersen, K. Deppert, H. Bluhm, Z. Liu, M. E. Grass, M. Hävecker and E. Lundgren, *Physical Review B*, 2011, **83**, 115440–1–115440–10.

38 A. Cao, R. Lu and G. Veser, *Physical Chemistry Chemical Physics*, 2010, **12**, 13499–13510.

39 R. Feidenhans'l, *Surface Science Reports*, 1989, **10**, 105 – 188.

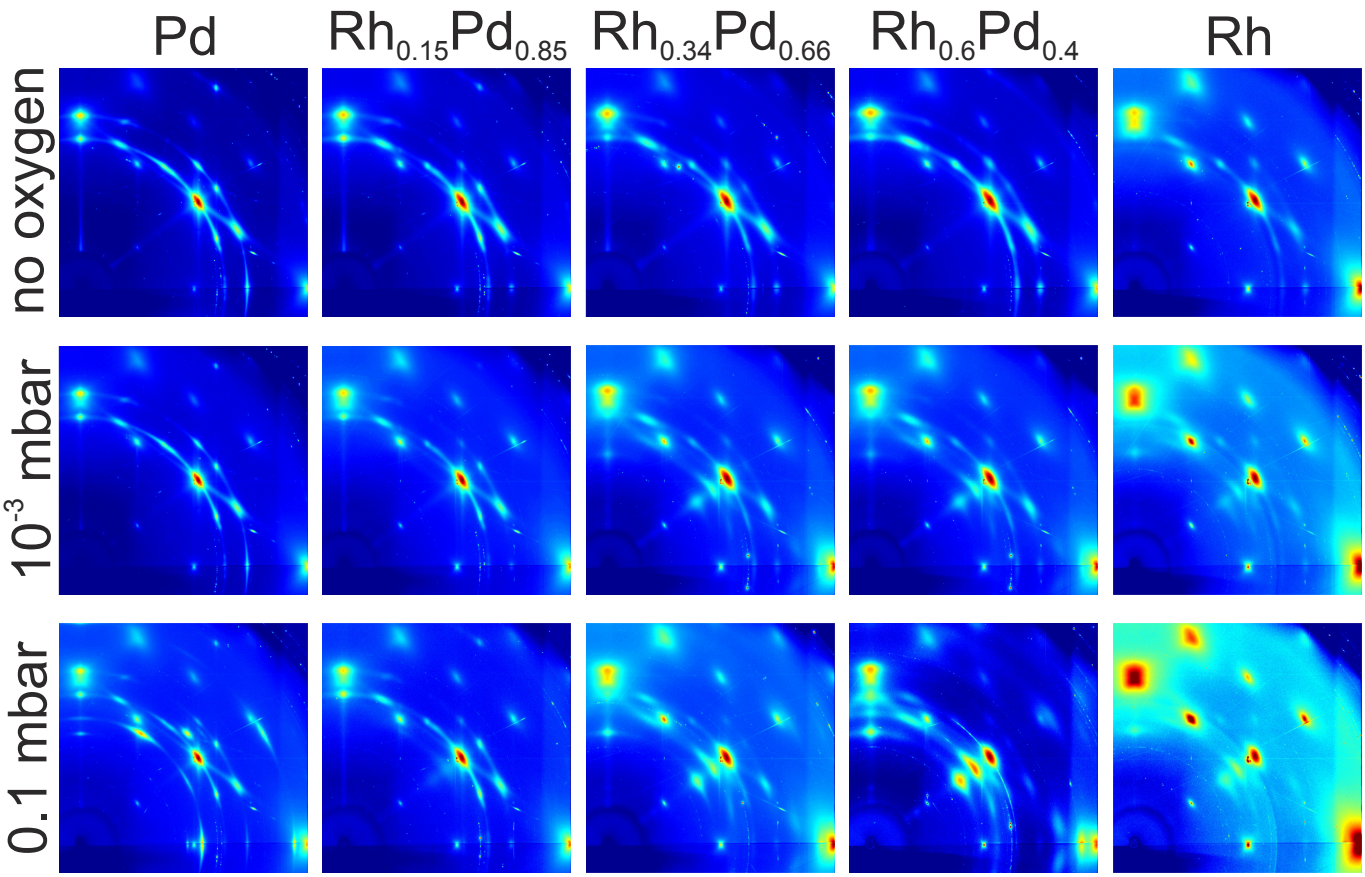

Fig. 4 2D diffraction patterns of the different nanoparticle stripes for UHV, 10^{-3} mbar O_2 and 10^{-1} mbar O_2 at T = 670 K. The counting time for the images ranged between 60 and 100 s. During oxygen exposure additional Bragg reflections appear, allowing for the identification of corresponding rhodium and palladium oxide phases.